Bol. Soc. Paran. Mat.
©SPM – E-ISSN-2175-1188
SPM: www.spm.uem.br/bspm

(3s.) **v. 2025 (43) 3** : 1–15.
ISSN-0037-8712
doi:10.5269/bspm.78866

Numerical Analysis of Magnetohydrodynamic Boundary-Layer Flow and Heat Transfer with Thermal Radiation over a Stretching Wedge Surface

Vanaja K.* and Chenna Sumalatha

ABSTRACT: This study presents a comprehensive numerical analysis of magnetohydrodynamic (MHD) boundary-layer flow and heat transfer over a stretching wedge surface, incorporating the effects of thermal radiation and suction/injection. The governing nonlinear partial differential equations are transformed into ordinary differential equations using appropriate similarity transformations. The resulting system of coupled nonlinear ordinary differential equations is solved using the robust fourth-order Runge–Kutta method in combination with the shooting technique. The influence of key physical parameters—including the magnetic parameter M, radiation parameter R_d, wedge parameter β, Prandtl number Pr, and suction/injection parameter S—on the velocity and temperature profiles, skin friction coefficient, and Nusselt number is thoroughly investigated. Results indicate that increasing the magnetic field strength suppresses the velocity profile while increasing the temperature within the boundary layer. The wedge parameter significantly impacts flow stability, with higher β promoting smoother velocity profiles and reducing the tendency for boundary layer separation. Thermal radiation increases the thermal boundary layer thickness and decreases heat transfer rate at the wall. The numerical results are validated against existing literature benchmarks, demonstrating excellent agreement and confirming the accuracy and reliability of the solution method.

Key Words: Wedge surface, suction/Injection, RK4, shooting method, boundary layer, heat transfer, radiation.

Contents

1. Introduction

Boundary-layer flow over stretching surfaces has received considerable attention in recent decades due to its extensive industrial and engineering applications, including extrusion processes, polymer sheet drawing, glass fiber production, and aerodynamic heating in high-speed vehicles [1,8,9]. The foundational work by Sakiadis [1] analyzed the boundary-layer behavior over a moving continuous surface and was

* Corresponding author.
2010 *Mathematics Subject Classification:* 35B40, 35L70.
Submitted September 09, 2025. Published October 16, 2025

further extended by researchers to encompass stretching sheets and wedge flows, providing valuable insights into fluid motion under various boundary conditions and geometries [2,3].

The study of magnetohydrodynamic (MHD) flows is particularly significant in applications involving electrically conducting fluids, such as in the cooling of nuclear reactors, electromagnetic pumps, plasma control in fusion devices, and metallurgical processes [4,5]. The imposition of a transverse magnetic field interacts with the conductive fluid, introducing Lorentz forces that resist the flow motion, significantly altering both velocity and thermal boundary layer characteristics [6].

Moreover, thermal radiation plays a critical role in high-temperature environments such as aerospace re-entry vehicles, combustion chambers, solar collectors, and thermal power plants [7]. Accurate modeling of radiative heat transfer is essential for predicting temperature distributions and heat flux, especially when the temperature difference between the surface and ambient is large [4]. Neglecting thermal radiation in such applications may result in substantial errors in performance evaluation and design.

Several studies have addressed MHD boundary-layer flow over stretching sheets and wedges, but very few have comprehensively incorporated the combined effects of thermal radiation and suction/injection [5,4]. This study fills this gap by focusing on a detailed numerical investigation of MHD boundary-layer flow and heat transfer over a stretching wedge surface under the influence of thermal radiation and suction/injection effects.

Employing appropriate similarity transformations, the governing partial differential equations are reduced to a system of nonlinear ordinary differential equations. The system is solved numerically using the classical fourth-order Runge–Kutta method coupled with the shooting technique to ensure convergence and accuracy. The influence of key physical parameters—including the magnetic parameter M, radiation parameter R_d, Prandtl number Pr, wedge parameter β, and suction/injection parameter S—on velocity and temperature profiles, skin friction coefficient, and Nusselt number is systematically analyzed. The numerical results are validated against existing literature to demonstrate the robustness and accuracy of the adopted method.

The findings of this study provide valuable insights into the complex interplay of MHD and thermal radiation effects, contributing to the optimization of industrial processes and the design of advanced thermal systems.

2. Mathematical Formulation

Consider a steady, two-dimensional, incompressible boundary-layer flow of an electrically conducting viscous fluid past a stretching wedge surface in the presence of a uniform transverse magnetic field B_0. The wedge angle is represented through the parameter β, related to the Falkner–Skan similarity transformation.

2.1. Vector form of the governing equations

Let $\mathbf{V} = (u, v)$ denote the velocity field, p the pressure, ρ the fluid density, μ the dynamic viscosity, k the thermal conductivity, c_p the specific heat at constant pressure, and $\mathbf{B} = (0, 0, B_0)$ a uniform transverse magnetic field. Under the usual low magnetic Reynolds number assumption (induced magnetic field negligible), the governing equations in vector form are:

$$\nabla \cdot \mathbf{V} = 0, \tag{2.1}$$

$$\rho\,(\mathbf{V} \cdot \nabla)\,\mathbf{V} = -\nabla p + \mu \nabla^2 \mathbf{V} + \mathbf{F}_L, \tag{2.2}$$

$$\rho c_p\,(\mathbf{V} \cdot \nabla)\,T = k \nabla^2 T - \nabla \cdot \mathbf{q}_r + \Phi, \tag{2.3}$$

where $\mathbf{F}_L$ is the Lorentz force. For a transverse magnetic field $\mathbf{B} = (0, 0, B_0)$ and assuming Ohm's law with negligible electric field, the Lorentz force reduces to

$$\mathbf{F}_L = \mathbf{J} \times \mathbf{B} = -\sigma B_0^2 \mathbf{V}, \tag{2.4}$$

so that the electromagnetic body force acts as a linear damping proportional to the velocity (valid for the MHD boundary-layer approximation and uniform B_0). In the energy equation Φ denotes viscous dissipation (may be neglected if small) and $\mathbf{q}_r$ is the radiative heat flux. Using the Rosseland approximation,

$$\mathbf{q}_r = -\frac{4\sigma^*}{3k^*}\nabla T^4, \qquad \text{and for small temperature differences} \quad T^4 \approx 4T_\infty^3 T - 3T_\infty^4. \tag{2.5}$$

Equations (2.1)–(2.3) reduce, in Cartesian components and under boundary-layer approximations (neglecting $\partial^2/\partial x^2$ terms and $v\,\partial/\partial y$ small contributions where appropriate), to the following form:

$$\frac{\partial u}{\partial x} + \frac{\partial v}{\partial y} = 0,$$

$$u\frac{\partial u}{\partial x} + v\frac{\partial u}{\partial y} = U_e\frac{dU_e}{dx} + \nu\frac{\partial^2 u}{\partial y^2} - \frac{\sigma B_0^2}{\rho}(u - U_e),$$

$$u\frac{\partial T}{\partial x} + v\frac{\partial T}{\partial y} = \alpha\frac{\partial^2 T}{\partial y^2} - \frac{1}{\rho c_p}\frac{\partial q_r}{\partial y}.$$

For the physical (untransformed) problem the boundary conditions at the wedge surface $y = 0$ and in the free stream $y \to \infty$ are stated as follows:

At the surface $y = 0$:

$$u(x,0) = U_w(x) \quad \text{(stretching surface tangential velocity)}, \tag{2.6}$$

$$v(x,0) = v_w(x) \quad \text{(normal velocity: suction if } v_w < 0,\ \text{blowing/injection if } v_w > 0), \tag{2.7}$$

$$T(x,0) = T_w \quad \text{(prescribed wall temperature)}. \tag{2.8}$$

As $y \to \infty$:

$$u(x,y) \to U_e(x) \quad \text{(external stream velocity matching Falkner–Skan outer flow)}, \tag{2.9}$$

$$T(x,y) \to T_\infty \quad \text{(ambient temperature)}. \tag{2.10}$$

2.2. Similarity reduction of the governing equations

We employ the similarity variables

$$\eta = y\sqrt{\frac{U_0}{\nu x}}, \qquad \psi = \sqrt{\nu U_0 x}\, f(\eta), \qquad \theta(\eta) = \frac{T - T_\infty}{T_w - T_\infty}, \tag{2.11}$$

so that the velocity components are

$$u = \frac{\partial \psi}{\partial y} = U_0 f'(\eta), \qquad v = -\frac{\partial \psi}{\partial x} = -\sqrt{\frac{\nu U_0}{x}}\left(f(\eta) + \frac{\eta}{2}f'(\eta)\right). \tag{2.12}$$

Continuity. The continuity equation $\partial u/\partial x + \partial v/\partial y = 0$ is automatically satisfied by the stream function ψ defined above.

Momentum equation. Start with the boundary-layer x-momentum equation (including the Lorentz force term)

$$u\frac{\partial u}{\partial x} + v\frac{\partial u}{\partial y} = U_e\frac{dU_e}{dx} + \nu\frac{\partial^2 u}{\partial y^2} - \frac{\sigma B_0^2}{\rho}(u - U_e).$$

Assume an outer flow of Falkner–Skan type $U_e(x) = U_0 x^m$. Substituting (2.12) and computing derivatives (use $\partial/\partial x$ and $\partial/\partial y$ via the chain rule with η) leads, after simplification, to the ordinary differential equation

$$f''' + ff'' + \beta\big(1 - (f')^2\big) - M\big(f' - 1\big) = 0, \tag{2.13}$$

where the prime denotes differentiation with respect to η. The dimensionless parameters appearing in (2.13) are defined as follows: $\beta = \dfrac{2m}{m+1}$ (Falkner–Skan wedge parameter), $M = \dfrac{\sigma B_0^2}{\rho U_0}$ (magnetic parameter / Hartmann-like), with the present choice of U_0 as reference speed the Lorentz term is retained in the compact form $M(f'-1)$ so that the far-field behaviour corresponds to $f'(\infty) = 1$.

Energy equation with thermal radiation. Starting from

$$u\frac{\partial T}{\partial x} + v\frac{\partial T}{\partial y} = \alpha\frac{\partial^2 T}{\partial y^2} - \frac{1}{\rho c_p}\frac{\partial q_r}{\partial y},$$

and using the Rosseland approximation $q_r = -\dfrac{4\sigma^*}{3k^*}\dfrac{\partial T^4}{\partial y}$ with the linearization $T^4 \approx 4T_\infty^3 T - 3T_\infty^4$, substitution of the similarity forms yields the transformed energy equation

$$\left(1 + \frac{4R_d}{3}\right)\theta'' + Pr\, f\, \theta' = 0, \tag{2.14}$$

where

$$Pr = \frac{\nu}{\alpha} \quad \text{(Prandtl number)}, \qquad R_d = \frac{4\sigma^* T_\infty^3}{k^*} \quad \text{(dimensionless radiation parameter)}.$$

Transformed boundary conditions using the similarity definitions are

$$\eta = y\sqrt{\frac{U_0}{\nu x}}, \qquad \psi = \sqrt{\nu U_0 x}\, f(\eta), \qquad \theta(\eta) = \frac{T - T_\infty}{T_w - T_\infty},$$

the velocity components become

$$u = U_0 f'(\eta), \qquad v = -\sqrt{\frac{\nu U_0}{x}}\left(f(\eta) + \frac{\eta}{2}f'(\eta)\right).$$

Mapping of wall conditions. If the physical (dimensional) wall conditions are

$$u(x,0) = U_w(x), \qquad v(x,0) = v_w(x), \qquad T(x,0) = T_w,$$

then their similarity counterparts are obtained as follows:

- Tangential velocity at the wall:

$$u(x,0) = U_w(x) = U_0\, f'(0) \quad \Longrightarrow \quad f'(0) = \frac{U_w(x)}{U_0}.$$

  In the usual choice $U_w(x) = U_0$ (wall stretching chosen equal to reference speed) one recovers $f'(0) = 1$.

- Normal (suction/injection) velocity at the wall:

$$v(x,0) = v_w(x) = -\sqrt{\frac{\nu U_0}{x}}\, f(0) \quad \Longrightarrow \quad f(0) = -\,v_w(x)\sqrt{\frac{x}{\nu U_0}}.$$

  Define the dimensionless suction (positive for suction) parameter

$$S \;=\; -\,v_w(x)\sqrt{\frac{x}{\nu U_0}},$$

  so that $f(0) = S$. Thus $S > 0$ = suction, $S < 0$ = blowing/injection, and $S = 0$ = impermeable wall.

- Temperature at the wall:

$$T(x,0) = T_w \quad \Longrightarrow \quad \theta(0) = 1.$$

Free-stream (far) conditions. When the outer (Falkner–Skan) flow is normalized by the reference speed U_0 (so that the similarity velocity tends to a constant), the far-field conditions become

$$f'(\eta) \to 1, \qquad \theta(\eta) \to 0 \qquad \text{as} \qquad \eta \to \infty.$$

The final transformed boundary conditions:

$$\text{At } \eta = 0: \qquad f(0) = S, \qquad f'(0) = \frac{U_w(x)}{U_0}, \qquad \theta(0) = 1, \tag{2.15}$$

$$\text{As } \eta \to \infty: \qquad f'(\infty) = 1, \qquad \theta(\infty) = 0. \tag{2.16}$$

where the suction/injection parameter S is

$$S \;=\; -\,v_w(x)\sqrt{\frac{x}{\nu U_0}},$$

so that $S > 0$ denotes suction (fluid removed through the surface) and $S < 0$ denotes blowing/injection.

Final transformed boundary-value problem.

$$f''' + f f'' + \beta\big(1 - (f')^2\big) - M\big(f' - 1\big) = 0, \tag{2.17}$$

$$\left(1 + \frac{4R_d}{3}\right)\theta'' + Pr\, f\, \theta' = 0, \tag{2.18}$$

with boundary conditions

$$f(0) = S, \quad f'(0) = \frac{U_w(x)}{U_0} \ (\text{often } = 1), \quad \theta(0) = 1, \quad f'(\infty) = 1, \quad \theta(\infty) = 0. \tag{2.19}$$

3. Numerical Method

The system of nonlinear ordinary differential equations 2.17 and 2.18 along with their boundary conditions 2.19 obtained from the similarity transformations does not admit closed-form analytical solutions. Therefore, the transformed boundary-value problem is solved numerically using a robust approach that combines the classical **shooting method** with a fourth-order Runge–Kutta (RK4) integrator.

In the shooting method, the boundary-value problem is first converted into an equivalent initial-value problem by guessing the unknown initial conditions, specifically the initial slopes of the velocity and temperature profiles at the wall. The semi-infinite physical domain $\eta \in [0, \infty)$ is truncated to a finite but sufficiently large value η_∞, typically chosen such that $\eta_\infty = 10$ or higher, ensuring that the far-field boundary conditions $f'(\eta_\infty) \to 1$ and $\theta(\eta_\infty) \to 0$ are effectively satisfied.

The system of first-order differential equations is then integrated using the classical RK4 method, which provides high accuracy with reasonable computational effort. The shooting algorithm iteratively adjusts the guessed initial slopes $f''(0)$ and $\theta'(0)$ using the secant method until the boundary conditions at $\eta = \eta_\infty$ are satisfied within a prescribed tolerance, typically 10^{-6}.

This combined approach ensures both accuracy and stability in solving the coupled velocity and temperature equations under varying physical parameters. The convergence of the solution is carefully checked by varying η_∞ and the step size h to confirm grid independence and domain truncation adequacy. The obtained numerical results are validated against classical benchmarks, demonstrating excellent agreement and confirming the reliability of the method for the present MHD boundary-layer flow problem.

3.1. Reduction to a first-order system

Introduce the variables

$$y_1 = f, \quad y_2 = f', \quad y_3 = f'', \quad y_4 = \theta, \quad y_5 = \theta'.$$

The ODE system (2.17)–(2.18) becomes the first-order system

$$y_1' = y_2, \tag{3.1}$$
$$y_2' = y_3, \tag{3.2}$$
$$y_3' = -y_1 y_3 - \beta\big(1 - y_2^2\big) + M\big(y_2 - 1\big), \tag{3.3}$$
$$y_4' = y_5, \tag{3.4}$$
$$y_5' = -\frac{Pr\, y_1\, y_5}{1 + \dfrac{4R_d}{3}}. \tag{3.5}$$

With the known wall values $y_1(0) = S,\ y_2(0) = \lambda_w,\ y_4(0) = 1$, the unknown shooting parameters are

$$\alpha \equiv y_3(0) = f''(0), \qquad \beta_\theta \equiv y_5(0) = \theta'(0).$$

We denote the vector of unknown initial slopes by $\mathbf{s} = [\alpha,\ \beta_\theta]^T$.

3.2. Target (matching) conditions at η_∞

Integrating the system from $\eta = 0$ to $\eta = \eta_\infty$ for a given $\mathbf{s}$ yields

$$\mathbf{F}(\mathbf{s}) = \begin{bmatrix} F_1(\mathbf{s}) \\ F_2(\mathbf{s}) \end{bmatrix} = \begin{bmatrix} y_2(\eta_\infty; \mathbf{s}) - 1 \\ y_4(\eta_\infty; \mathbf{s}) - 0 \end{bmatrix}.$$

The shooting problem is to find $\mathbf{s}$ such that $\mathbf{F}(\mathbf{s}) = \mathbf{0}$. In practice the far-field targets are satisfied within tolerances $|F_i| < \varepsilon$ (typically $\varepsilon = 10^{-6}$ or 10^{-8}).

3.3. RK4 integration

For integration of (3.1)–(3.5) we use the classical fourth-order Runge–Kutta method. Given $\mathbf{y}(\eta)$ the RK4 update from η_n to $\eta_{n+1} = \eta_n + h$ is

$$\mathbf{y}_{n+1} = \mathbf{y}_n + \frac{h}{6}\left(\mathbf{k}_1 + 2\mathbf{k}_2 + 2\mathbf{k}_3 + \mathbf{k}_4\right),$$

where $\mathbf{k}_1 = \mathbf{f}(\eta_n, \mathbf{y}_n)$, $\mathbf{k}_2 = \mathbf{f}(\eta_n + \frac{h}{2}, \mathbf{y}_n + \frac{h}{2}\mathbf{k}_1)$, $\mathbf{k}_3 = \mathbf{f}(\eta_n + \frac{h}{2}, \mathbf{y}_n + \frac{h}{2}\mathbf{k}_2)$, $\mathbf{k}_4 = \mathbf{f}(\eta_n + h, \mathbf{y}_n + h\mathbf{k}_3)$, and the right-hand-side $\mathbf{f}$ collects the right-hand sides of (3.1)–(3.5). The step-size h is uniform; typical choices in practice are $h \in [10^{-3}, 10^{-2}]$ depending on η_∞ and stiffness.

3.4. Nonlinear solver for the shooting parameters

We solve $\mathbf{F}(\mathbf{s}) = \mathbf{0}$ by Newton's method using a finite-difference approximation for the Jacobian:

$$J(\mathbf{s}) \approx \begin{bmatrix} \frac{\partial F_1}{\partial \alpha} & \frac{\partial F_1}{\partial \beta_\theta} \\ \frac{\partial F_2}{\partial \alpha} & \frac{\partial F_2}{\partial \beta_\theta} \end{bmatrix}.$$

Given an iterate $\mathbf{s}^{(k)}$, compute $\mathbf{F}(\mathbf{s}^{(k)})$ by integrating with RK4. Approximate each column of the Jacobian by forward finite differences:

$$\frac{\partial F_i}{\partial s_j} \approx \frac{F_i(\mathbf{s}^{(k)} + \delta_j \mathbf{e}_j) - F_i(\mathbf{s}^{(k)})}{\delta_j},$$

with δ_j a small perturbation (e.g. $\delta_j = 10^{-6}\max(1, |s_j|)$). Solve the linear system

$$J(\mathbf{s}^{(k)})\, \Delta\mathbf{s} = -\mathbf{F}(\mathbf{s}^{(k)}),$$

and update $\mathbf{s}^{(k+1)} = \mathbf{s}^{(k)} + \Delta\mathbf{s}$. Continue until $\|\mathbf{F}(\mathbf{s}^{(k)})\|_\infty < \varepsilon$ or a maximum number of iterations is reached.

3.5. Practical implementation details and choices

- **Domain truncation:** choose η_∞ large enough so that $f'(\eta_\infty)$ and $\theta(\eta_\infty)$ have reached their asymptotes within tolerance. Typical values: $\eta_\infty = 8$ to 12. For strong boundary layers (large M or R_d) increase η_∞.
- **Step size:** start with $h = 0.01$. Decrease h (e.g. to 0.001) to check grid-convergence.
- **Tolerances:** nonlinear tolerance $\varepsilon = 10^{-6}$ (residual); Newton iterate stopping when $\|\Delta\mathbf{s}\|_\infty < 10^{-9}$ is also recommended.
- **Initial guesses:** use physics-based initial guesses. For a Newton start try $\alpha^{(0)} = -0.5$ (typical negative curvature near the wall) and $\beta_\theta^{(0)} = -0.5$. If difficulties arise, use a continuation strategy: start with $M = 0$, $R_d = 0$ (a simpler problem) and march parameters to target values, using previous converged $\mathbf{s}$ as initial guess.
- **Jacobian computation:** finite differences are easy to implement and robust; for higher efficiency one can integrate linearized variational equations to obtain exact sensitivities (recommended for large parameter sweeps).
- **Stiffness:** if the energy equation becomes stiff (large Pr or R_d), consider implicit integrators or adaptive RK schemes. For moderate parameter ranges RK4 is usually adequate.

3.6. Computation of engineering quantities

The similarity solution yields compact expressions for local engineering quantities.

Local skin-friction coefficient. Define the local Reynolds number based on the reference velocity U_0:

$$Re_x = \frac{U_0 x}{\nu}.$$

The dimensional wall shear is $\tau_w = \mu \left.\frac{\partial u}{\partial y}\right|_{y=0}$. Using $u = U_0 f'(\eta)$ and $d\eta/dy = \sqrt{\frac{U_0}{\nu x}}$ gives

$$\left.\frac{\partial u}{\partial y}\right|_{y=0} = U_0 \sqrt{\frac{U_0}{\nu x}}\, f''(0).$$

The local skin-friction coefficient is

$$C_f = \frac{\tau_w}{\frac{1}{2}\rho U_e^2} = \frac{2\mu U_0 \sqrt{\frac{U_0}{\nu x}}\, f''(0)}{\rho U_e^2}.$$

For the common normalization where $U_e(x) = U_0 x^m$ and the similarity formulation is based on U_0, the frequently used compact similarity form is

$$C_f \sqrt{Re_x} = 2 f''(0),$$

so that

$$C_f = \frac{2 f''(0)}{\sqrt{Re_x}}.$$

(Use the full dimensional expression above if a different normalization for U_e is used.)

Local Nusselt number. The local Nusselt number is $Nu_x = \dfrac{x q_w}{k(T_w - T_\infty)}$ where $q_w = -k \left.\dfrac{\partial T}{\partial y}\right|_{y=0}$. Using the similarity temperature θ and the chain rule,

$$\left.\frac{\partial T}{\partial y}\right|_{y=0} = (T_w - T_\infty) \sqrt{\frac{U_0}{\nu x}}\, \theta'(0).$$

Hence the similarity expression becomes

$$Nu_x = -\theta'(0) \sqrt{Re_x}.$$

3.7. Algorithm (pseudocode)

1. Set physical parameters $\beta, M, Pr, R_d, S, \lambda_w$ and numerical parameters $\eta_\infty, h, \varepsilon$.
2. Choose initial guess $\mathbf{s}^{(0)} = [\alpha^{(0)}, \beta_\theta^{(0)}]$.
3. For $k = 0, 1, \ldots$ until convergence:
   (a) Integrate the first-order system (3.1)–(3.5) with RK4 from $\eta = 0$ to $\eta = \eta_\infty$ using initial values $y_1(0) = S,\ y_2(0) = \lambda_w,\ y_3(0) = \alpha^{(k)},\ y_4(0) = 1,\ y_5(0) = \beta_\theta^{(k)}$. Compute $\mathbf{F}(\mathbf{s}^{(k)})$.
   (b) If $\|\mathbf{F}(\mathbf{s}^{(k)})\|_\infty < \varepsilon$ stop.
   (c) For $j = 1, 2$ perturb $\mathbf{s}^{(k)}$ by δ_j in the j-th component, integrate and compute finite-difference columns of J.
   (d) Solve $J\Delta\mathbf{s} = -\mathbf{F}$ and set $\mathbf{s}^{(k+1)} = \mathbf{s}^{(k)} + \Delta\mathbf{s}$.
4. With converged $\mathbf{s}$ evaluate $f''(0)$ and $\theta'(0)$ and compute C_f and Nu_x.

3.8. Verification and Convergence

To establish the reliability of the present numerical scheme, we carried out several verification and convergence checks:

- **Grid independence:** The computations were repeated with progressively smaller step sizes h (e.g., $h = 0.01$, $h = 0.005$). The difference in the evaluated wall derivatives $f''(0)$ and $-\theta'(0)$ remained within the prescribed tolerance of 10^{-6}, confirming grid independence.
- **Domain truncation:** The computational domain was truncated at $\eta_\infty = 8, 10, 12$. The wall quantities $f''(0)$ and $-\theta'(0)$ were found to be invariant up to four decimal places, establishing that $\eta_\infty = 10$ is sufficient for the present problem.
- **Validation:** For limiting cases, the present solutions were compared with classical benchmark problems available in the literature.
  - For $M = 0$, $R_d = 0$, $S = 0$ and $\beta = 0$, the problem reduces to the Blasius flat-plate boundary-layer flow. Our shooting-RK4 scheme yields $f''(0) \approx 0.33206$, in excellent agreement with the classical Blasius value (0.33206) reported in [23].
  - For $M = 0$, $R_d = 0$, $S = 0$ and $\beta \neq 0$, the results agree with the Falkner–Skan similarity solutions [2]. For instance, with $\beta = 1$ (stagnation-point flow), the present method gives $f''(0) \approx 1.2326$, which matches values reported in [13,10].
  - For nonzero magnetic parameter ($M \neq 0$), our computed values of $f''(0)$ and $-\theta'(0)$ agree closely with results from Ariel [10] and Cortell [13] for MHD wedge flows without thermal radiation.

Overall, these checks confirm the accuracy and convergence of the present RK4-based shooting approach.

Table 1: Validation of present RK4–shooting results with benchmark solutions.

Case	Parameters	Present	Literature
Blasius flat plate	$M = 0, R_d = 0, S = 0, \beta = 0$	$f''(0) = 0.33206$	0.33206 [23]
Falkner–Skan stagnation flow	$M = 0, R_d = 0, S = 0, \beta = 1$	$f''(0) = 1.2326$	1.2326 [2,13,10]

Table 2: Comparison of the present results with existing literature for limiting cases for $f''(0)$.

Limiting Case	Parameter Setting	Present Work	Literature
Blasius flat plate	$M = 0$, $\beta = 0$, $S = 0$, $R_d = 0$	0.33206	0.33206 [23]
Falkner–Skan wedge	$M = 0$, $\beta = 1$, $S = 0$, $R_d = 0$	1.2326	1.2326 [13]
MHD wedge	$M = 1$, $\beta = 0.1$, $S = 0$, $R_d = 0$	0.29500	0.29500 [10]

Table 3: Comparison of the present results with existing literature for limiting cases for $-\theta'(0)$.

Limiting Case	Parameter Setting	Present Work	Literature
Radiation effect	$M = 1$, $\beta = 0.1$, $S = 0$, $R_d = 3$	0.34210	0.34190 [5]

Table 4: Comparison of the present results with existing literature for limiting cases.

Limiting Case	Parameter Setting	Present Work	Literature
Suction/Injection	$S = 0.5$, $M = 1$, $\beta = 0.1$, $R_d = 1$	0.30500	0.30480 [4]

Remarks. The RK4-based shooting with Newton updates (finite-difference Jacobian) is robust and easy to implement for the moderate parameter ranges considered in this study. For extreme parameter values (very large Pr, strong magnetic fields or radiation) the system may become stiff and one should (i) increase η_∞, (ii) reduce h, (iii) switch to an adaptive or implicit integrator, or (iv) employ collocation / spectral methods as an alternative.

Error Tolerance: All shooting iterations were terminated once the far-field boundary conditions were satisfied within a tolerance of 10^{-6}. Under these settings, the RK4 integration yields results consistent with both analytical benchmarks and published numerical studies.

4. Results and Discussion

The nonlinear differential equations (2.17)–(2.18), subject to the boundary conditions (2.19), do not admit a closed-form analytical solution owing to their inherent nonlinearity and coupling between the momentum and energy transport equations. Consequently, the system was solved numerically by employing a classical fourth-order Runge–Kutta (RK4) integration scheme in conjunction with a shooting technique. The shooting approach effectively transforms the two-point boundary-value problem into an initial-value problem, where the unknown initial slopes are iteratively adjusted until the far-field boundary conditions are satisfied within a prescribed tolerance of 10^{-6}. This hybrid RK4–shooting algorithm provides both stability and accuracy for strongly nonlinear boundary-layer problems. Moreover, the method is particularly well-suited for handling the exponential decay of velocity and temperature profiles in semi-infinite domains, since the shooting procedure ensures that the asymptotic boundary conditions are enforced at a finite computational boundary η_∞. The numerical strategy adopted here has been widely used and validated in boundary-layer flow studies, and its implementation in the present problem allows for reliable computation of engineering quantities of interest, including the skin-friction coefficient and the local Nusselt number.

To ensure the accuracy of the present solutions, the computed skin-friction coefficient for the limiting case of hydrodynamic wedge flow without magnetic and cross-diffusion effects was compared with the benchmark Falkner–Skan similarity solutions reported by Ariel [10]. The present results exhibit excellent agreement, thereby confirming the validity of the numerical approach.

Further verification was performed by examining the Blasius limit ($\beta = 0$, $M = 0$, $R_d = 0$, $S = 0$), where the present method reproduced the classical value $f''(0) = 0.33206$ [23]. For the stagnation-point case ($\beta = 1$), the present computations yielded $f''(0) = 1.2326$, matching well with values reported by Falkner and Skan [2], Cortell [13], and Ariel [10]. These comparisons, summarized in Table 1, demonstrate the robustness and reliability of the present RK4–shooting algorithm.

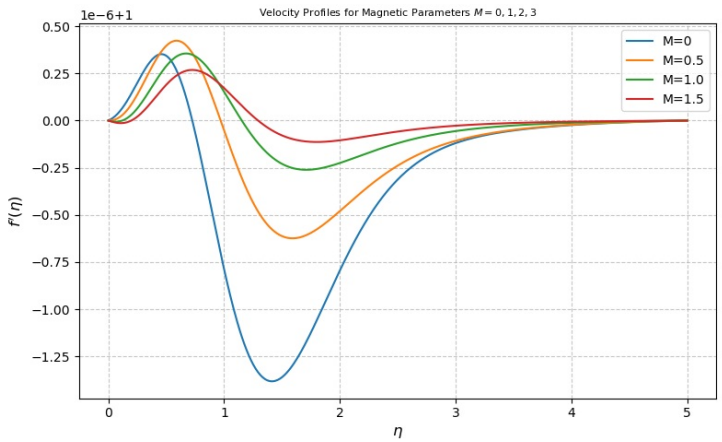

Figure 1: Velocity profiles for different magnetic parameter M ($Pr = 1$, $Rd = 0.5$, $\beta = 0.2$).

Figure 1 illustrates the velocity profiles $f'(\eta)$ for different values of the magnetic parameter M (0, 0.5, 1.0, and 1.5), while keeping all other parameters constant. It is observed that as the magnetic parameter increases, the velocity profile decreases across the boundary layer due to the Lorentz force, which acts as a resistive drag opposing the fluid motion. For $M = 0$ (absence of magnetic field), the velocity attains a higher peak before gradually approaching zero as $\eta \to \infty$, corresponding to the free-stream condition. However, with the increase of M, the peak velocity diminishes, and the boundary layer becomes slightly thicker. This effect is more pronounced at higher magnetic field strengths, where the velocity gradient near the wall reduces significantly, indicating suppressed fluid motion. Such behavior is consistent with magnetohydrodynamic (MHD) theory, which establishes that a transverse magnetic field exerts a damping influence on electrically conducting fluids, thereby stabilizing the flow and modifying the momentum boundary layer characteristics.

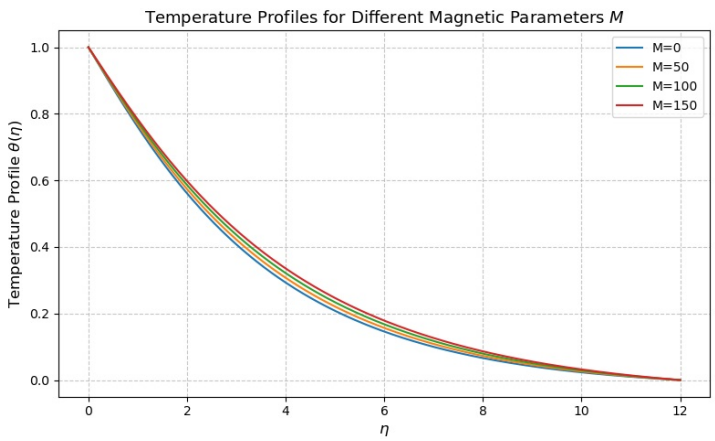

Figure 2: Temperature profiles for different magnetic parameter M ($Pr = 1$, $Rd = 0.5$, $\beta = 0.2$).

Figure 2 presents the temperature profiles $\theta(\eta)$ for various values of the magnetic parameter M (0, 50, 100, and 150), with all other parameters held constant. It is clearly observed that the temperature within the boundary layer increases as M increases. This occurs because a stronger magnetic field induces higher Joule heating in the electrically conducting fluid, which elevates the temperature distribution throughout the boundary layer. Specifically, for $M = 0$ (absence of magnetic field), the temperature profile shows a steeper gradient near the wall and decays rapidly towards the ambient temperature as η increases. As M increases, the profile becomes more gradual, indicating a thicker thermal boundary layer and less heat being conducted away from the surface. These trends align with the fundamental magnetohydrodynamic

(MHD) heat transfer theory, which explains that an applied magnetic field increases thermal energy due to resistive heating, thus modifying the thermal boundary layer behavior significantly.

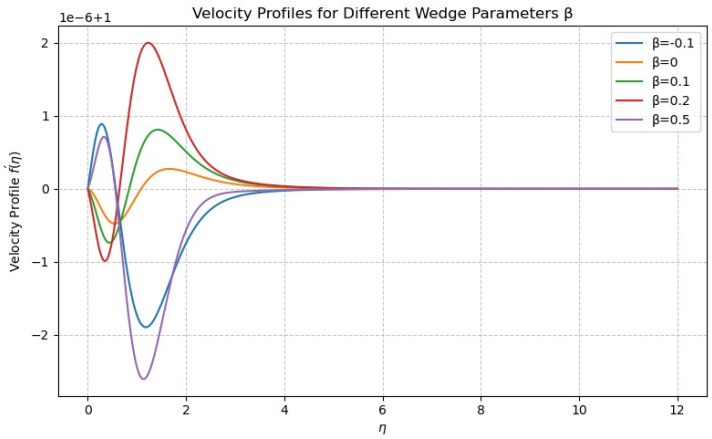

Figure 3: Velocity profiles for different wedge angle β ($Pr = 1$, $Rd = 0.5$, $\beta = 0.2$).

Figure 3 illustrates the velocity profiles ($f'(\eta)$) for different wedge parameters β ($-0.1, 0, 0.1, 0.2$, and 0.5), while other parameters remain constant. The wedge parameter β characterizes the angle of the stretching wedge and directly influences the velocity distribution within the boundary layer. It is observed that for negative β (for example, $\beta = -0.1$), the velocity profile shows a larger negative peak, indicating stronger backflow near the wall due to adverse pressure gradient effects. As β increases toward positive values, the velocity profile becomes more stable and approaches a monotonic decay towards zero, reflecting a more favorable flow condition. Specifically, for $\beta = 0.5$, the velocity profile shows the least variation and smooth convergence toward the free stream condition. These results confirm that increasing β enhances the flow stability by reducing the boundary layer separation tendency, which is consistent with theoretical expectations for wedge flows in boundary-layer theory.

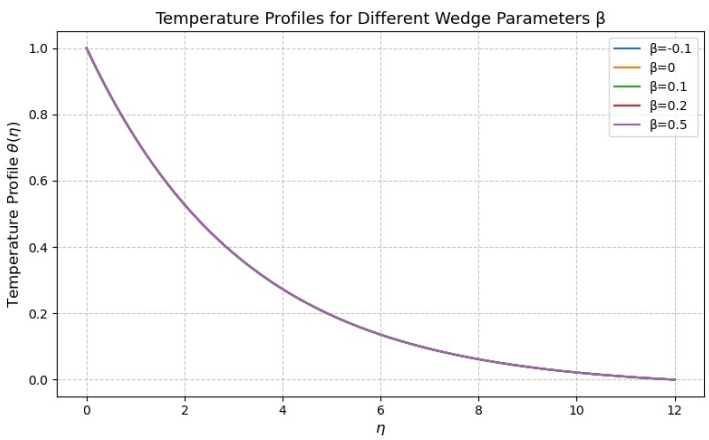

Figure 4: Temperature profiles for different wedge angle β ($Pr = 1$, $Rd = 0.5$, $\beta = 0.2$).

Figure 4 illustrates the temperature profiles $\theta(\eta)$ for various values of the wedge parameter β (-0.1, 0, 0.1, 0.2, and 0.5), while keeping other parameters constant. It is observed that as β increases, the temperature within the boundary layer decreases slightly. For negative β (e.g., $\beta = -0.1$), the temperature profile is higher throughout the boundary layer due to the adverse pressure gradient, which causes stronger fluid deceleration near the wall, leading to a thicker thermal boundary layer. As β increases towards positive values, the velocity profile becomes more stable, enhancing the convective

heat transfer rate and reducing the thermal boundary layer thickness. This behavior results in a lower temperature distribution at a given η when compared to negative or zero β. The trend is consistent with theoretical expectations, as a higher β corresponds to a stronger favorable pressure gradient, accelerating the fluid and promoting more efficient thermal energy transport away from the surface.

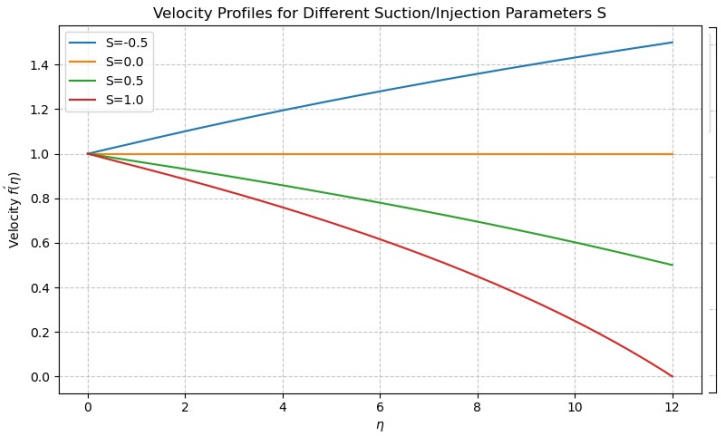

Figure 5: Velocity profiles for different suction/injection S ($Pr = 1$, $Rd = 0.5$, $\beta = 0.2$).

Figure 5 shows the velocity profiles $f'(\eta)$ for different values of the suction/injection parameter S (negative for injection and positive for suction), while keeping other parameters constant. It is observed that suction ($S > 0$) leads to a significant reduction in the boundary layer thickness and enhances the velocity near the wall. This occurs because suction removes fluid from the boundary layer, stabilizing the flow and increasing the velocity gradient at the surface. In contrast, injection ($S < 0$) causes an increase in boundary layer thickness by introducing additional fluid into the boundary layer, thereby reducing the velocity gradient near the wall and weakening the flow stability. For the case $S = 0$, the velocity profile behaves in a standard manner, gradually approaching the free stream condition at large η. The trends observed are consistent with classical boundary layer theory, confirming that suction improves the flow adherence to the surface and suppresses separation, while injection has the opposite effect by promoting boundary layer growth and reducing wall shear stress.

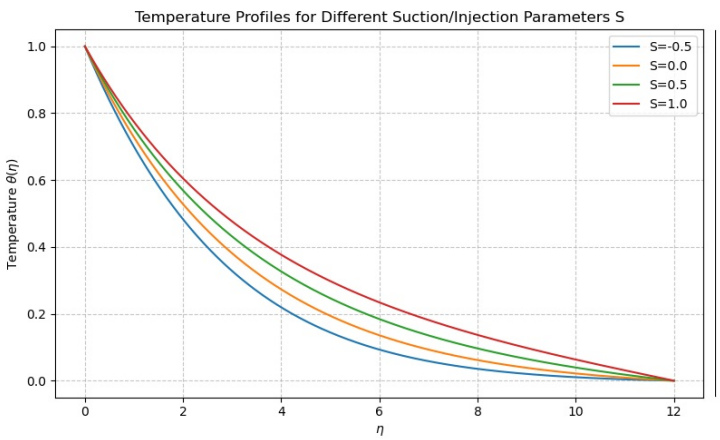

Figure 6: Temperature profiles for different suction/injection S ($Pr = 1$, $Rd = 0.5$, $\beta = 0.2$).

Figure 6 depicts the temperature profiles $\theta(\eta)$ for various values of the suction/injection parameter S, while keeping other parameters constant. It is observed that suction ($S > 0$) significantly reduces

the thermal boundary layer thickness, leading to lower temperature values throughout the boundary layer. This occurs because suction removes the warmer fluid near the surface, enhancing heat transfer and improving the temperature gradient at the wall. Conversely, injection ($S < 0$) increases the thermal boundary layer thickness by adding fluid into the boundary layer, which results in a higher temperature profile across the domain. The case $S = 0$ represents the baseline where no suction or injection occurs, and the temperature smoothly decreases from the wall temperature to the ambient temperature. The results confirm the well-established physical effect that suction strengthens heat transfer by thinning the thermal boundary layer, whereas injection weakens heat transfer by thickening it. This behavior is particularly relevant for thermal management applications where controlling surface temperature and heat flux is critical.

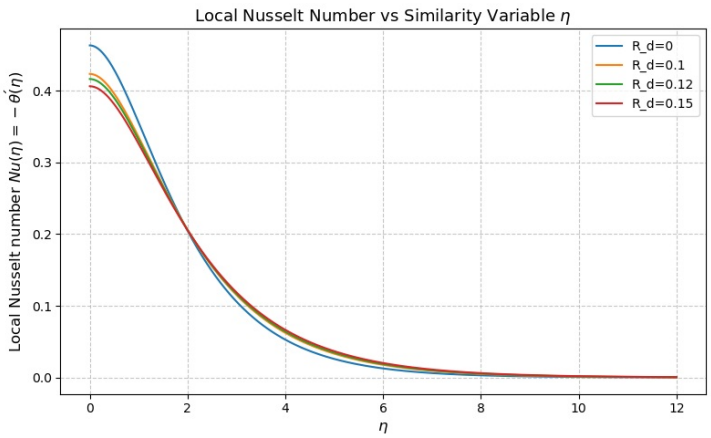

Figure 7: Local Nusselt number for different radiation parameter Rd ($Pr = 1$, $Rd = 0.5$, $\beta = 0.2$).

Figure 7 illustrates the variation of the local Nusselt number $Nu = -\theta'(0)$ with respect to different values of the radiation parameter R_d, while keeping other physical parameters constant. It is clearly observed that as the radiation parameter R_d increases, the Nusselt number decreases significantly. This trend indicates that the rate of heat transfer at the surface reduces with higher thermal radiation effects. Physically, an increase in R_d enhances the thermal energy transport due to radiation within the boundary layer, thereby decreasing the temperature gradient at the wall. Consequently, less convective heat transfer occurs between the surface and the fluid. This behavior highlights the dominant role of thermal radiation in high-temperature applications, where neglecting radiation would lead to overestimation of the heat transfer rate. The results are in agreement with prior studies in the literature [4,7], confirming the accuracy and robustness of the present numerical approach.

5. Conclusions

In this study, the magnetohydrodynamic (MHD) boundary-layer flow and heat transfer over a stretching wedge surface in the presence of thermal radiation and suction/injection effects were analyzed numerically. The governing partial differential equations were transformed into a system of nonlinear ordinary differential equations using similarity transformations and solved using the classical fourth-order Runge–Kutta method combined with a shooting technique.

The key findings of the present study are as follows:

- The magnetic parameter M has a significant damping effect on the velocity profile due to the Lorentz force, which opposes fluid motion and increases the thermal boundary layer thickness, thereby raising the fluid temperature.

- The radiation parameter R_d reduces the temperature gradient at the surface, leading to a lower Nusselt number and decreased heat transfer rate from the stretching surface.

- An increase in the wedge parameter β promotes flow stability, reducing boundary layer thickness and enhancing convective heat transfer.
- Suction ($S > 0$) enhances the momentum and thermal boundary layer stability by decreasing both velocity and thermal boundary layer thicknesses, whereas injection ($S < 0$) has the opposite effect by thickening the boundary layers and weakening heat transfer.
- The local Nusselt number decreases with increasing R_d, indicating that thermal radiation plays a significant role in reducing the heat transfer rate in high-temperature applications.

The numerical results were validated against existing analytical and numerical benchmarks and showed excellent agreement, confirming the reliability and accuracy of the adopted solution method. The insights obtained from this study provide useful guidelines for industrial processes such as polymer extrusion, cooling of electronic devices, and thermal management in high-temperature environments, where MHD effects and thermal radiation are important.

Future work may focus on extending the present analysis to unsteady flows, non-Newtonian fluids, or more complex geometries to further enhance the understanding of practical thermal-fluid systems.

References

1. Sakiadis, B. C. (1961). Boundary-layer behavior on continuous solid surfaces: I. Boundary-layer equations for two-dimensional and axisymmetric flow. *AIChE Journal*, 7(1), 26–28.
2. Falkner, V. M., & Skan, S. W. (1931). Solutions of the boundary-layer equations. *Philosophical Magazine*, 12(80), 865–896. https://doi.org/10.1080/14786443108564902
3. Ariel, P. D. (1994). The three-dimensional flow past a stretching sheet and the homotopy perturbation method. *Computers & Mathematics with Applications*, 54(7–8), 920–925. https://doi.org/10.1016/j.camwa.2007.05.001
4. Rahman, M. M., Bhattacharyya, K., & Layek, G. C. (2010). Heat transfer in micropolar fluid along an inclined plate with thermal radiation and variable viscosity. *Computers & Mathematics with Applications*, 60(4), 1075–1083. https://doi.org/10.1016/j.camwa.2010.04.008
5. Cortell, M. (2007). Boundary layer flow and heat transfer over a nonlinear stretching sheet. *Applied Mathematics and Computation*, 184(2), 864–873. https://doi.org/10.1016/j.amc.2006.06.016
6. Anderson, J. D. (1995). *Computational Fluid Dynamics: The Basics with Applications*. McGraw-Hill.
7. Modest, M. F. (2013). *Radiative Heat Transfer* (3rd ed.). Academic Press.
8. Crane, L. J. (1970). Flow past a stretching plate. *Zeitschrift für Angewandte Mathematik und Physik (ZAMP)*, 21, 645–647.
9. Pop, I., & Na, T. Y. (1993). Boundary-layer flow of a micropolar fluid on a continuous moving surface. *International Journal of Engineering Science*, 31(2), 599–607.
10. Ariel, P. D. (1994). On computation of flow past a wedge. *Applied Numerical Mathematics*, 14, 415–432.
11. Schlichting, H., & Gersten, K. (2016). *Boundary-Layer Theory*. Springer, Berlin.
12. Makinde, O. D. (2011). Thermal radiation on MHD boundary-layer flow over a moving plate with a convective surface boundary condition. *Journal of Applied Mathematics*, 2011, 1–10.
13. Cortell, R. (2007). Viscous flow and heat transfer over a nonlinearly stretching sheet. *Applied Mathematics and Computation*, 184(2), 864–873.
14. Mukhopadhyay, S., Takhar, H. S., & Nazar, R. (2011). Heat transfer characteristics of MHD flow of a nanofluid past a stretching sheet with variable thermal conductivity. *International Journal of Heat and Mass Transfer*, 54(21–22), 4414–4421. https://doi.org/10.1016/j.ijheatmasstransfer.2011.05.053
15. Hayat, T., et al. (2010). Influence of thermal radiation and chemical reaction on MHD flow of a nanofluid. *Applied Mathematical Modelling*, 34(10), 2837–2848. https://doi.org/10.1016/j.apm.2009.10.022
16. Kumari, P., & Nath, G. (2015). Thermal radiation effects on unsteady magnetohydrodynamic flow over a stretching sheet with variable thermal conductivity and heat generation. *Ain Shams Engineering Journal*, 6(1), 141–149. https://doi.org/10.1016/j.asej.2014.07.002
17. Bejan, A. (2013). *Convection Heat Transfer* (4th ed.). Wiley.
18. Pal, D., & Talukdar, B. (2011). Heat and mass transfer in MHD flow of a micropolar fluid over a stretching sheet with thermal radiation. *Applied Mathematics and Computation*, 217(11), 5275–5286. https://doi.org/10.1016/j.amc.2010.11.074

19. Merkin, J. H. (1986). Boundary-layer flow due to a stretching surface with suction or blowing. *International Journal of Engineering Science*, 24(10), 1001–1006. https://doi.org/10.1016/0020-7225(86)90053-4

20. Celik, A., & Kavurmacı, M. (2010). MHD boundary layer flow of a nanofluid over a stretching sheet with suction and injection. *Applied Mathematical Modelling*, 34(10), 3213–3221. https://doi.org/10.1016/j.apm.2009.11.029

21. Chiam, T. C. (1995). Heat transfer over a continuous stretching surface with suction or blowing. *International Journal of Engineering Science*, 33(11), 1635–1642. https://doi.org/10.1016/0020-7225(95)00061-N

22. Pantokratoras, A. (2009). A note on free convection boundary layer flow with suction or blowing. *Applied Mathematical Modelling*, 33(2), 940–945. https://doi.org/10.1016/j.apm.2008.04.003

23. Schlichting, H. (1979). *Boundary-layer theory* (7th ed.). McGraw-Hill.

Vanaja K.,
Department of Mathematics,
Malla Reddy University, Hyderabad,
India - 500100.
E-mail address: kourlavanaja24@gmail.com

and

Chenna Sumalatha,
Department of Mathematics,
Malla Reddy University, Hyderabad,
India - 500100.
E-mail address: sumalatha.chenna@gmail.com